

An imaging study of a complex solar coronal radio eruption

S. W. Feng^{1,2}, Y. Chen¹, H. Q. Song¹, B. Wang¹, X. L. Kong¹

ABSTRACT

Solar coronal radio bursts are enhanced radio emission excited by energetic electrons accelerated during solar eruptions, studies on which are important for investigating the origin and physical mechanism of energetic particles and further diagnosing coronal parameters. Earlier studies suffered from a lack of simultaneous high-quality imaging data of the radio burst and the eruptive structure in the inner corona. Here we present a study on a complex solar radio eruption consisting of a type II and three reversely-drifting type III bursts, using simultaneous EUV and radio imaging data. It is found that the type II burst is closely associated with a propagating and evolving CME-driven EUV shock structure, originated initially at the northern shock flank and later transferred to the top part of the shock. This source transfer is co-incident with the presence of shock decay and enhancing signatures observed at the corresponding side of the EUV front. The electron energy accelerated by the shock at the flank is estimated to be $\sim 0.3 c$ by examining the imaging data of the fast-drifting herringbone structure of the type II burst. The reversely-drifting type III sources are found to be within the ejecta and correlated with a likely reconnection event therein. Implications on further observational studies and relevant space-weather forecasting techniques are discussed.

Subject headings: – Sun: corona – Sun: activity – Sun: coronal mass ejections (CMEs) – Sun: radio radiation

1. Introduction

Coronal radio bursts at metric wavelength are observational manifestation of energetic electrons that are accelerated in the solar atmosphere. These radio bursts, carrying valuable information about how energetic particles are accelerated and the underlying emission

¹Shandong Provincial Key Laboratory of Optical Astronomy and Solar-Terrestrial Environment, and Institute of Space Sciences, Shandong University, Weihai, Shandong 264209, China; yaochen@sdu.edu.cn

²State Key Laboratory of Space Weather, Chinese Academy of Sciences, Beijing 100190, China

mechanism, can be used to infer parameters of coronal magnetic field and plasmas, which otherwise remain difficult to measure with other techniques.

Among various types of coronal radio bursts, the type II, narrow and slowly-drifting bands on the solar radio dynamic spectrum, is believed to be excited by energetic electrons accelerated at coronal shocks. It has been discovered (Allen 1947; Payne-Scott 1947) and studied for nearly 70 years, yet major issues, such as where and how the electrons are accelerated by a shock and how some fine structures (e.g., splitting bands, see latest studies by Vasanth et al. 2014 and Du et al. 2014, 2015, and herringbones, see e.g., Cairns & Robinson 1987) are formed, remain unresolved. Regarding the relative source location on the shock surface, earlier studies claimed that both the nose front and the flank of a shock can be sources of type IIs (Reiner et al. 2003; Cho et al. 2007, 2008; Feng et al. 2012, 2013; Kong et al. 2012; Chen et al. 2014). These studies, providing valuable insights into the type II origin, are mostly based on non-imaging spectrometric data of the radio burst and low-cadence white-light data of the coronal mass ejection (CME). Considering metric radio bursts occur within 2-3 solar radii from the solar center (as inferred from their frequencies) with a relatively short duration of several to ~ 10 minutes, direct imaging data of the metric t-II source are not available for most events analyzed earlier.

This situation has changed with the availability of the high-cadence high-sensitivity Atmospheric Imaging Assembly on board the Solar Dynamics Observatory (AIA/SDO) instrument (Lemen et al. 2012; Pesnell et al. 2012) with EUV passbands covering a broad range of plasma temperatures, together with the ground-based solar radio heliograph instrument working in the metric wavelength, especially the Nançay Radio Heliograph (NRH, Kerdraon & Delouis 1997). In latest studies, these two sets of imaging data have been combined to reveal more insights into the physics of metric radio bursts, not only type II (Feng et al. 2015; Zimovets, et al. 2015; Eselevich, et al. 2015), but also type IV radio bursts (Tun & Vourlidas 2013, Bain et al. 2014, Vasanth et al. 2016) among others. For example, Feng et al. (2015) investigated the source regions of a three-lane type II burst, and found that all lanes are located at the shock flank with two lanes on the southern part and the other one from a distinct location on the northern part, consistent with the result obtained by Zimovets et al. (2015) on the same event.

Latest numerical studies on the role of the large-scale closed magnetic field in shock-electron acceleration suggest that the relative curvature of the shock and the closed field across which the shock is crossing is important to the efficiency of electron acceleration (Kong et al. 2015, 2016). They further deduced that at low shock altitudes, when the shock is more curved than the interacting closed magnetic field, the electrons are mainly accelerated at the shock flank; at higher altitudes, when the shock is less curved, the electrons are mainly

accelerated at the shock nose around the top of the closed field lines. Both the local shock geometry (being quasi-parallel or quasi-perpendicular, with the latter being expected to be more efficient in electron acceleration (Wu et al. 1984)) and the trapping effect of closed field lines play a role in the described process. This predicts a shift of efficient electron acceleration site along the shock front and a transfer of corresponding radio emitting sources from the flank to the top during the shock propagation. Such a transfer of radio sources along a coronal shock has not been reported, to the best of our knowledge.

Another topic of particular interest here is related to the type III radio burst, which corresponds to fast drifting features on the dynamic spectrum, being one of the **best** understood type of coronal radio bursts. The type III burst is thought to be excited by fast electron beams propagating along open or open-like (i.e., large-scale closed) field lines via the classical plasma emission mechanism (Ginzburg & Zhelezniakov 1958, Melrose 1980). The energetic electrons are usually believed to be accelerated by magnetic reconnection accounting for solar flares at the base of the corona. Besides the usual type III burst drifting from higher to lower frequencies, reversely-drifting or even bi-directional type III bursts are sometimes observed, with the other component that drifts from lower to higher frequencies (Aschwanden et al. 1993, 1995; Robinson & Benz 2000; Ning et al. 2000; Tan et al. 2016). These type IIIs are regarded as a sensitive tool to diagnose the physical conditions around the magnetic energy release site where reconnection and particle acceleration take place, **studies on which suffer from the general lack of simultaneous radio and EUV imaging data.**

Here we present an observational study on a complex coronal radio burst characterized by both type II and reversely-drifting type III bursts. It is associated with a solar eruption observed from the limb in the AIA field of view (FOV), and the accompanying EUV shock structure is clearly observable. Simultaneous NRH data at several metric wavelengths from 445 to 228 MHz are also available. Interesting results about the radio sources and its connection to the underlying eruptive processes are obtained.

2. Observational data and event overview

For the dynamic spectra we used the data recorded by the ORFEES spectrometer at the Nançay observatory at higher frequency (1 GHz - 140 MHz) and the San Vito data of the Radio Solar Telescope Network (RSTN) at lower frequency (140 - 25 MHz). The associated eruption is imaged by the AIA/SDO in different EUV passbands with a 12s cadence and a pixel size of 0.6", and the radio sources are imaged by the NRH from 150-445 MHz with spatial resolution depending on the imaging frequency ($\sim 1'.2'$ at 445 MHz, decreasing to

5'-6' at 150 MHz).

The event is associated with an M5.9 class flare on 24 August 2014, which starts at 12:00 UT, peaks at 12:17 UT and ends at 12:25 UT according to the GOES SXR data. It is from the NOAA active region (AR 12151, S09E76) and accompanied by a filament eruption on the limb which further evolves into a CME with a linear speed of 550 km s^{-1} according to the Large Angle Spectroscopic Coronagraph (Brueckner et al. 1995) C2 data. From AIA, the erupting filament presents a nice Ω -shape morphology, indicating the occurrence of the flux rope kink instability (Török & Kliem 2005). Song et al. (2015) presented a dynamical analysis on the event and found that the filament experiences a two-step fast acceleration phases with the first one not and the second one corresponding to a significant increase of HXR profiles. They thus suggested that the first acceleration phase is driven by the energy release dominated by ideal flux rope instability and the second phase dominated by flare-related magnetic reconnection. The amounts of energy release of the two steps are comparable, consistent with earlier numerical simulation (Chen et al. 2007).

Here we focus on the AIA EUV wave fronts which are driven by and propagate ahead of the eruptive filament. See Figure 1 for the evolutionary sequence of the wave structure observed at 211 \AA . The front has a circular shape in the projection plane. Its temporal evolution can be viewed from Figure 1, the accompanying online animation, and the distance-time maps along the two slices S1 and S2 (see Figure 2). Before 12:11:16 UT (see Figure 1a-1b), the front along S1 exhibits a complex multi-**shell** structure, while at $\sim 12:12 \text{ UT}$ and later (Figure 1c-1h), the multi-**shell** structure is pushed forward by the ejecta and steepens into a single-**shell** bright structure. This may indicate the formation of the shock there, as confirmed later by the presence of co-spatial type II radio sources. While examining the EUV wave evolution at the lateral side, we find that at $\sim 12:10 \text{ UT}$, the wave there is already single-**shell**, a result of earlier super-radial lateral expansion of the eruptive structure. This may indicate the formation of the shock structure is about two minutes earlier at the flank than at the top part. After 12:12:23 UT (Figure 1d), the EUV wave at the flank near the Sun ($< 1.1 R_{\odot}$) becomes diffuse and not recognizable later, indicating possible decay of the shock there. The EUV wave morphological evolution is in line with the radio data to be presented. The propagation speeds as measured from the slice maps are $\sim 120 \text{ km s}^{-1}$ for the EUV wave flank from 12:10 to 12:12 UT, slower than the speed at the nose front of the EUV wave ($\sim 600 \text{ km s}^{-1}$) as measured from 12:12 to 12:14 UT.

The dynamic spectra of the event is shown in Figure 3a. It is a complex event consisting of several types of radio bursts. From high to low frequencies, there are the first episode of the type III ($\sim 12:03 \text{ UT}$) just 3 minutes after the flare start, its second episode (from 12:10 - 12:16 UT) that embeds within the type-IV continuum. At their low-frequency end, the

type III and IV bursts are enveloped by a narrow and relatively slowly-drifting band of type II. At the lower end of the type II, a cluster of type I with sporadic brightenings appearing from 200 to 250 MHz after 12:10 UT. At lower frequencies, the emission is dominated by a second episode of type II with split bands and fundamental-harmonic branches.

3. Imaging the type II radio burst and its herringbone structure

Now we focus on the bursts shown in Figure 3b, corresponding to the box region of Figure 3a. We can see that the high-frequency type II band is characterized by discontinuous and fragmented emission, consisting of many fast drifting herringbone structures. The NRH total brightness temperatures (T_B) at frequencies from 445 to 228 MHz, normalized by the corresponding maximum T_B , are superposed to show the nice correlation between the NRH data and the spectral data. Along the type II band, we select eight spectral points (indicated by crosses in Figure 3b) at which the NRH T_B peaks. The corresponding type II sources have been superposed onto the AIA data in Figure 1.

The most important radio-source information **visible in** Figure 1 is the shift of type II sources with time. From the first three panels and before 12:11:59 UT, the type II sources are located at the flank of the EUV wave, indicating the shock presence there. In Figure 1(d), the type II source appears at the top part of the EUV wave and stays there later. The time of the source shift occurs between 12:11:50 to 12:12:20 UT. During this interval, the type II spectrum presents some discontinuity with a sharp change of frequency, possibly associated with the shift. As mentioned earlier, the source shift is in line with the EUV wave morphological evolution, as shown in Figures 1 and 2. There we see that before 12:12 UT the flank of the EUV wave (corresponding to the S2 map), where the type II sources were located then, shows a strong shock-like single-**shell** bright structure, while at the top part (corresponding to the S1 map) the multi-**shell** structure steepens into a single-**shell** shock-like feature after 12:12 UT, co-incident with the radio source jump from the flank to top.

As mentioned the type II backbone consists of fast drifting herringbone structures, which are suggested to be excited by fast energetic electrons accelerated at and escaped from the shock (Cairns & Robinson 1987). With the source images of the herringbone at different frequencies, one can estimate the speed of shock-released electrons. The herringbone structure usually occupies only a limited frequency range, so it is in general difficult to do this. Nevertheless, here we identify one such herringbone structure that is imaged by NRH at two frequencies at 408 and 327 MHz (see the red box region in Figure 3). The corresponding spectral data and NRH source contours are shown in Figure 4. Assuming that the peaks

of the radio flux correspond to the same beam of electrons, we can track their motion and estimate their speed. At 12:12:20 UT the electrons (and the herringbone source at 408 MHz) are at the flank, while ~ 1.5 s later (inferred from the timing difference of the two plus signs) the electrons move to the top part of the ejecta, so does the herringbone source at 327 MHz. It is not possible to determine the exact trajectory of the electron beam, yet we can obtain a lower estimate of the electron speed by assuming the distance between the source centroids (~ 200 arcsecs) to be the moving distance of the beam within the 1.5s interval. This gives a speed of ~ 0.3 c. Note that this should be regarded as a rough estimate mainly due to the limitation of the NRH spatial resolution. The herringbone structure appears during the source transfer (or jump) process and the AIA-observed shock decay at the flank, implicating a possible link among these phenomena.

4. Imaging the reversely-drifting type IIIs and the associated magnetic reconnection

Now we focus on the type III bursts within the white (blue) box region of Figure 3. We re-draw the spectrum in Figure 5a and 5b, and superpose the NRH sources at 432 MHz onto the AIA 304 Å images (see Figure 5h). We see that there are three sets of type III, each imaged by the NRH at channels of 408, 432, and 445 MHz. Examining the fluxes, we see that all these type IIIs present likely reversely-drifting characteristics, and for the middle one there seems to exist bi-directional drifting signature with the frequency at which the bi-directional drift starts being around ~ 450 -500 MHz.

From Figure 5h, we see that the 432 MHz sources of these type IIIs are located within the ejecta, which are spatially separated from the overlying EUV wave. This implies the emitting electrons may be accelerated by processes taking place within the ejecta and unrelated to the shock. To verify this **assumption**, we examine the AIA data at various wavelengths and indeed find a possible reconnection process there.

The blue arrows in Figure 5c and 5f point at a pair of parallel and straight filamentary structures that are stretched outward by the eruption. In Figure 5d and 5g, a retreating bright knot appears and the two straight structures get kinked (see the arrows). Later in Figure 5e and 5h, the left filamentary structure seems to get connected to a different part of the ejecta. These sudden dynamical morphology change, most clearly viewed from the accompanying movie, indicates the occurrence of reconnection, which is co-incident with the appearance of the three reversely-drifting type IIIs. These observations support that the type IIIs are excited by energetic electrons accelerated by reconnections taking place within the ejecta. To estimate the speed of type-III emitting electrons, we assume the reconnection

site is reasonably close to the source centroids of the 432 MHz emission, as supported by our deduction of the frequency range at which the bi-directional type III burst starts. Then, the height of the reconnection site is estimated to be ~ 100 arcsec, taken from the mean height of the three source centroids (see Figure 5h). The electron propagation time from the reconnection site to the solar limb can be estimated by measuring the duration of the three sets of reversely-drifting type III, this gives us an interval of 1-2 s (see the three pairs of short vertical arrows plotted on top of Figure 5a-5b). Thus, we get the electron speed to be $\sim 0.1 - 0.2 c$. This is at the energy level comparable to those accounting for the type II herringbone.

5. Summary and discussion

We analyzed a complex solar radio burst with a combining analysis on the AIA-EUV images and the NRH radio sources at multiple metric-wavelengths. We focused on the high-frequency type II and III bursts. The type II burst is characterized by discontinuous emissions and fast drifting herringbone structures. We find that the first part (before 12:12 UT) of the type II burst is originated from the lateral side of the EUV wave and the later part is originated from its top, indicating a transfer of radio sources. This transfer, taking place within ~ 30 s, is consistent with AIA signatures of the EUV wave steepening (indicative of shock generation) and diffuse (indicative of shock **decay**) at its lateral side and its top. Measurements on one embedding herringbone source allow us to estimate the speed and energy of electrons released from the shock, $\sim 0.3 c$ (~ 25 keV). For the type III bursts, we provide observational evidence to support that they correspond to sunward-drifting electron beams accelerated via magnetic reconnection occurring within the ejecta (one of them also presents likely signature of anti-sunward drifting, i.e., being a bi-directional one). The speed of these electron beams are estimated to be $0.1 - 0.2 c$.

The observation of the type II source transfer along a single type II drifting band has a significant implication to relevant studies using the type II spectral drift to infer coronal shock properties, especially the shock propagation speed. These studies assume the type II sources are carried outwards by the shock along a certain direction, and infer the shock speed with a prescribed coronal density model. On this basis, several space weather forecasting schemes are constructed (Smith & Dryer 1990, Fry et al. 2001, Zhao & Feng 2015). Here we show that the type II sources along a single band can move from the flank side to the top front, thus a single density model is not applicable to this kind of event. Note that limits of using type II spectral data with a fixed density model have been pointed out by many earlier studies (e.g., Gopalswamy et al. 2009, Liu et al. 2009, Cho et al. 2011), and several

studies demonstrated how the type II spectral shape can be affected by the coronal density structures along the shock-radio source path, resulting in special spectral characteristics such as spectral bumps (Feng et al. 2012, 2013) or break (Kong et al. 2012).

As mentioned in the introduction, Kong et al. (2016) predicted that the source of efficient electron acceleration and possible type II burst can shift from the shock flank to its top part, mainly due to the change of the relative curvature of the spherical shock and the closed magnetic field lines. In that study, the dynamical evolution of the shock structure and its coupling with the coronal background are not considered self-consistently. Here from the data we show that the shock dynamical evolutionary process such as its enhancement (or generation) and decay also plays a critical role in determining the electron acceleration and the type II source motion. Besides the above factor, the change of the shock geometry may also play a role here. Initially, the surrounding field lines near the sun at the northern flank may be radial and thus parallel to the shock front (i.e., being a quasi-perpendicular shock, expected to be efficient in electron acceleration), while later the shock top may become quasi perpendicular if the shock then is sweeping across some overlying closed magnetic loops. This likely change of geometry at different side of the shock during its evolution is also in line with the observed type-II source transfer.

The type III bursts of this event are enveloped by the type II bands, with a close temporal-spectral coincidence. This makes one suspect that these bursts are physically connected with a common origin at the EUV shock. However, we show that the type III burst is very likely related to the reconnection process occurring within the ejecta during the eruption. The reconnection in the corona results in bi-directional electron beams, with the outward-flowing electrons accounting for the NRH sources around 400 MHz, and the sunward-flowing electrons accounting for the high-frequency part. The latter may further excite X-ray emission when colliding with the lower solar atmosphere. To verify this, we examine the Ramaty High Energy Solar Spectroscopic Imager (RHESSI; Lin et al. 2002) data and found that the type IIIs are co-incident with strong rising X-ray emissions with oscillating light curves, it is thus not possible to identify the enhanced X-ray emission possibly associated with the type III emitting electrons. Further studies demand imaging data at higher-than-NRH frequencies for a better identification of the acceleration site and trajectory of electron beams.

We gratefully acknowledge the usage of data from the SDO-SOHO-RHESSI spacecraft and from the Nançay observatory and the RSTN. S. Feng thank Dr. Hui Fu for helpful discussion. This work was supported by grants NSBRSF 2012CB825601, NNSFC-CAS U1431103, and NNSFC 41331068, 41274175, 11503014, NSF of Shandong Province (ZR2013DQ004, ZR2014DQ001), and Project Supported by the Specialized Research Fund for the State Key

Laboratories.

REFERENCES

- Allen, C. W. 1974, MNRAS, 107, 386
- Aschwanden, M. J., Benz, A. O., Schwartz, R. A. 1993, ApJ, 417, 790
- Aschwanden, M. J., Benz, A. O., Dennis, B. R., Schwartz, R. A. 1995, ApJ, 455, 347
- Bain, H. M., Krucker, S., Saint Hilaire, P., Raftery, C. L. 2014, ApJ, 782, 43
- Brueckner, G. E., Howard, R. A., Koomen, M. J., et al. 1995, SoPh, 162, 357
- Cairns, I. H., & Robinson, R. D. 1987, SoPh, 111, 365
- Chen, Y., Hu, Y. Q., Sun, S. J. 2007, ApJ, 665, 1421
- Chen, Y., Du, G. H., Feng, L., et al. 2014, ApJ, 787, 59
- Cho, K. S., Lee, J., Moon, Y. J., Dryer, M., Bong, S. C., Kim, Y. H., Park, Y. D. 2007, A&A, 461, 1121
- Cho, K. S., Bong, S. C., Kim, Y. H., Moon, Y. J., Dryer, M., Shanmugaraju, A., Lee, J., Park, Y. D. 2008, A&A, 491, 873
- Cho, K. S., Bong, S. C., Moon, Y. J., Shanmugaraju, A., Kwon, R. Y., Park, Y. D. 2011, A&A, 530, 16
- Du, G. H., Chen, Y., Lv, M. S., et al. 2014, ApJL, 793, 39
- Du, G. H., Kong, X. L., Chen, Y., et al. 2015, ApJ, 812, 52
- Eselevich, V. G., Eselevich, M. V., Sadykov, V. M., Zimovets, I. V. 2015, AdSpR, 56, 2793
- Feng, S. W., Chen, Y., Kong, X. L., et al. 2012, ApJ, 753, 21
- Feng, S. W., Chen, Y., Kong, X. L., et al. 2013, ApJ, 767, 29
- Feng, S. W., Du, G. H., Chen, Y., et al. 2015, SoPh, 290, 1195
- Fry, C. D., Sun, W., Deehr, C. S., Dryer, M., Smith, Z., Akasofu, S. I., Tokumaru, M., Kojima, M. 2001, JGR, 106, 20985

- Ginzburg, V. L., & Zhelezniakov, V. V., 1958, SvA, 2, 653
- Gopalswamy, N., Thompson, W. T., Davila, J. M., Kaiser, M. L., Yashiro, S., Makela, P., Michalek, G., Bougeret, J. L., & Howard, R. A. 2009, SoPh, 259,227
- Kerdraon, A., Delouis, J. M. 1997, In: Trottet. G. (ed.), *Coronal Physics from Radio and Space Observations, Lecture Notes in Physics* 483, Springer, Berlin, 192.
- Kong, X. L., Chen, Y., Li, G., et al. 2012, ApJ, 750, 158
- Kong, X. L., Chen, Y., Guo, F., et al. 2015, ApJ, 798, 81
- Kong, X. L., Chen, Y., Guo, F., et al. 2016, ApJ, 821, 32
- Lemen, J. R., Title, A. M., Akin, D. J., Boerner, P. F., Chou, C., Drake, J. F. 2012, SoPh, 275, 17.
- Lin, R. P., Dennis, B. R., Hurford, G. J., et al. 2002, SoPh, 210, 3
- Liu, Y., Luhmann, J.G., Bale, S.D., Lin, R.P. 2009, ApJL, 691, L151
- Melrose, D. B. 1980, Plasma astrophysics, Vols. 1 and 2 (New York: Gordon and Breach)
- Ning, Z. J., Fu, Q. J., Lu, Q. K. 2000, SoPh, 194, 137
- Payne-Scott, R., Yabsley, D. E., Bolton, J. G. 1947, Nature, 160, 256
- Pesnell, W. D., Thompson, B. J., & Chamberlin, P. C. 2012, Sol. Phys., 275, 3
- Reiner, M. J., Vourlidas, A., Cyr, O. C. St., et al. 2003, ApJ, 590, 533
- Robinson, P. A., & Benz, A. O. 2000, SoPh, 194, 345
- Smith, Z., & Dryer, M. 1990, SoPh, 129, 387
- Song, H. Q., Chen, Y., Zhang, J., Cheng, X., Fu, H., Li, G. 2015, ApJL, 804, 38
- Tan, B. L., Mészárosóvá, H., Karlický, M., Huang, G. L., Tan, C. M. 2016, ApJ, 819, 42
- Török, T., & Kliem, B. 2005, ApJL, 630, 97
- Tun, S. D., & Vourlidas, A. 2013, ApJ, 766, 130
- Vasanth, V., Umapathy, S., Vrsnak, B., Zic, T., Prakash, O. 2014, SoPh, 289, 251

Vasanth, V., Chen, Y., Feng, S. W., Du, G. H., Song, H. Q., Kong X. L., Zheng, R. S. 2016,
submitted to ApJL

Wu, C. S. 1984, JGR, 89, 8857

Zhao, X. H., & Feng, X. S. 2015, ApJ, 809, 44

Zimovets, I. V., & Sadykov, V. M. 2015, AdSpR, 56, 2811

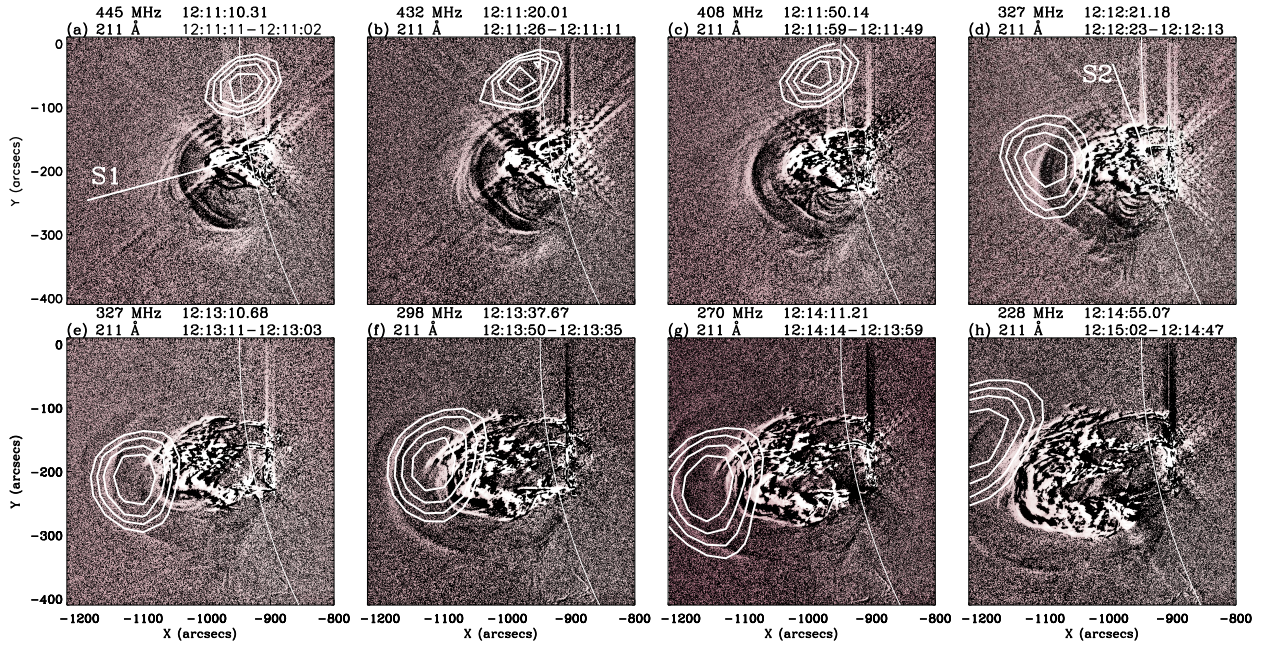


Fig. 1.— Temporal evolution of the EUV wave fronts, overlaid by the NRH type-II sources. The two slices S1 and S2 are for the distance-time maps to be shown in Figure 2. The type II sources are presented by contours levels of 95%, 90%, 85%, and 80% of the maximum T_B of each NRH image. An accompanying movie is available online.

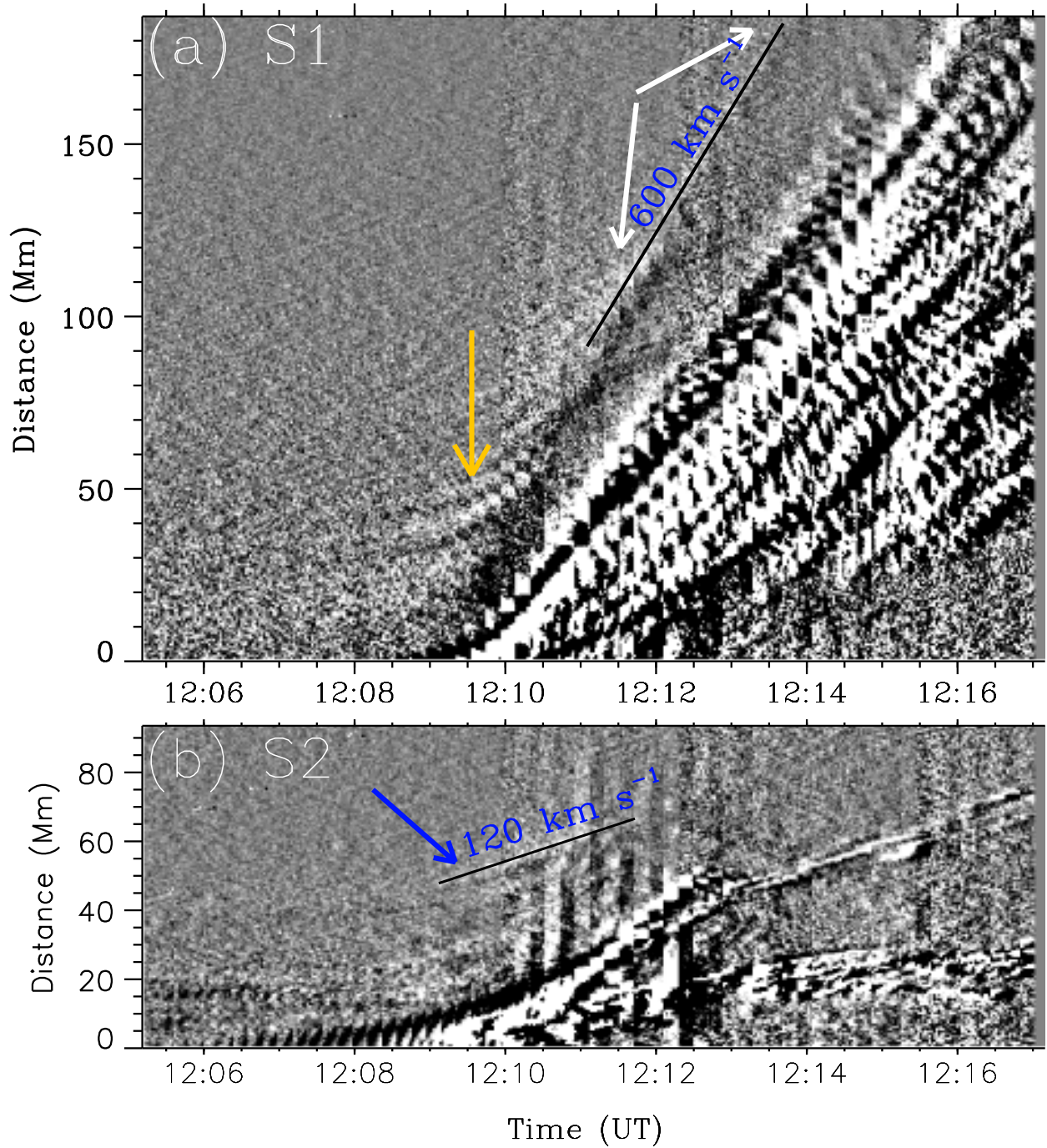


Fig. 2.— Distance-time maps along S1 (a) and S2 (b). The two arrows in (a) point to the multi-shell (yellow) and single-shell (white) structures. The speeds are given by linear fits of the distance measurements.

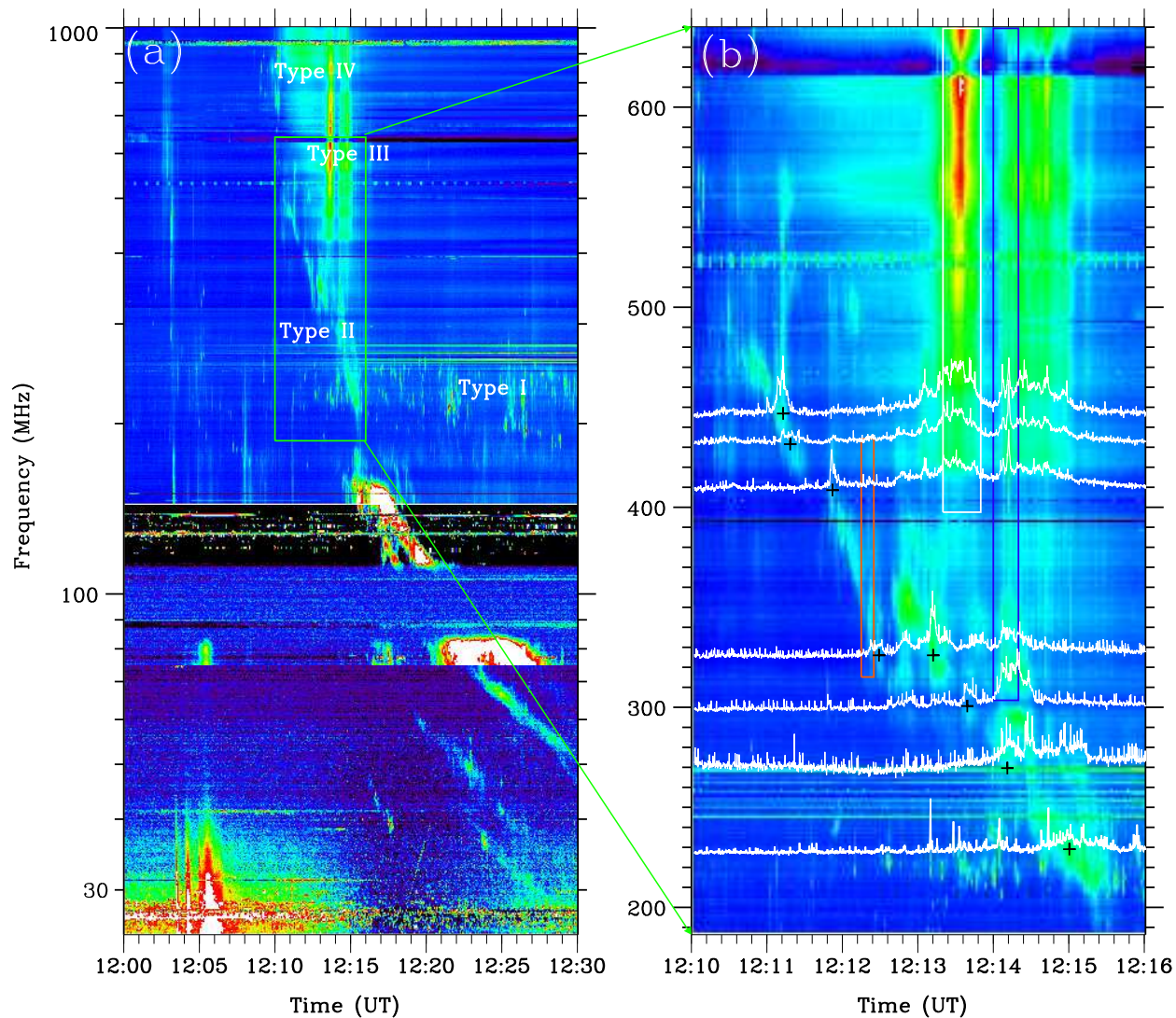


Fig. 3.— Dynamic spectra from ORFEES and SVTO/RSTN (a), with the box region shown in (b). The 8 pluses on the type II backbone in (b) indicate the normalized NRH flux peaks at different frequencies, with NRH sources already presented in Figure 1. The bottom level of these flux curves is placed at the corresponding NRH frequency on the y-axis. The red box around 12:12:20 UT is for the type II herringbone structure (see Figure 4), and the white and blue boxes around 12:13:30 and 12:14:10 UT are for the reversely drifting type III bursts (see Figure 5).

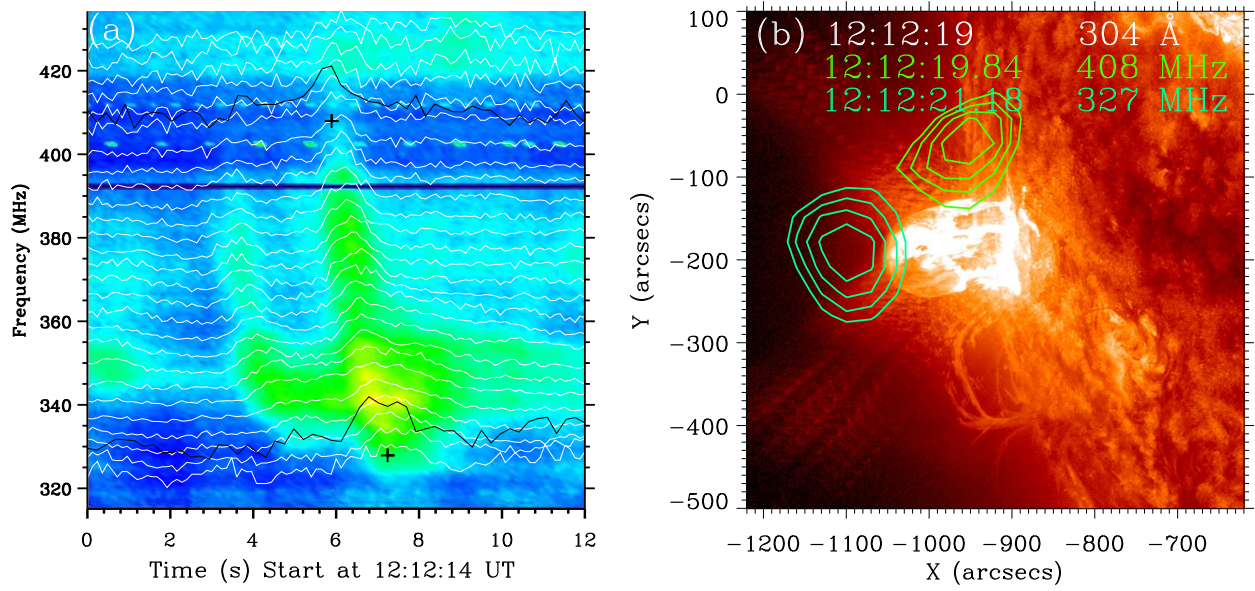


Fig. 4.— The spectral and imaging data for the type II herringbone (see the red box in Figure 3b). (a) The dynamic spectrum, over-plotted by the normalized T_B curves for the spectral data (white) and NRH fluxes at 408 and 327 MHz (black). The bottom levels of the curves are placed at the corresponding NRH frequency on the y-axis. The two pluses show the spectral locations of the radio sources presented in (b) with the AIA 304 Å image.

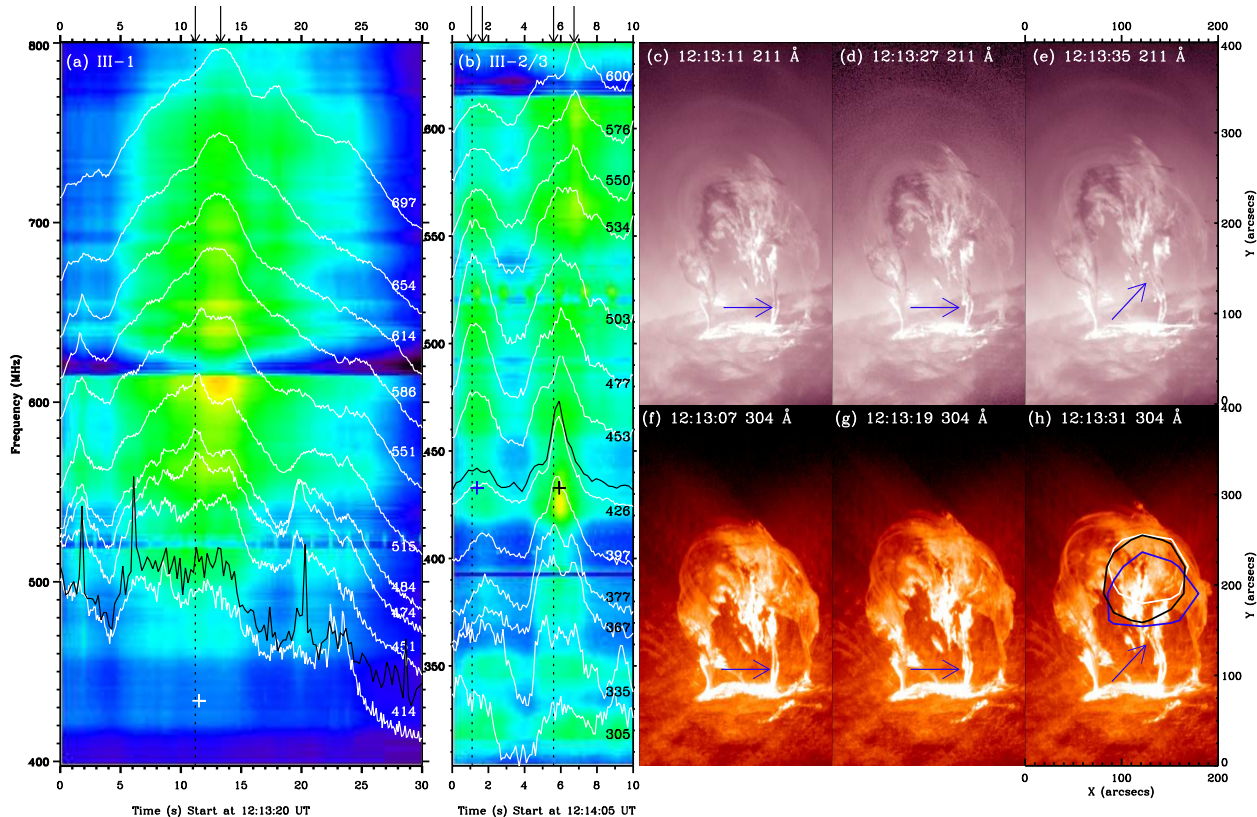


Fig. 5.— Radio spectral (a-b) and imaging data (c-h) for the three episodes of type IIIs. (a-b) Their dynamic spectra (see the white and blue boxes in Figure 3b), over-plotted by the normalized flux profiles (white) and NRH T_B curves (black). The three pluses show the selected points at 432 MHz at which the NRH sources are presented in panel (h). (c-h) The imaging sequence of AIA at 211 and 304 Å around 12:13 UT, to show the signature of the suspected reconnection within the ejecta. The arrows point to the pair of parallel filamentary structures and their morphology change. The pairs of vertical short arrows present the estimated durations of the reversely-drifting part of type IIIs. An accompanying movie is available online.